

# CERES\_EBAF-Surface\_Ed4.1 Data Quality Summary

Version 1  
Updated 6/15/2021

Investigation: CERES  
Data Product: EBAF-Surface

Data Set: Terra (Instruments: CERES-FM1 or CERES-FM2)  
Aqua (Instruments: CERES-FM3 or CERES-FM4)

Data Set Version: Edition4.1      Release Date: June 8, 2021

Subsetting Tool Availability: <https://ceres.larc.nasa.gov/data/>

The purpose of this document is to inform users of the accuracy of this data product as determined by the CERES Science Team. **This document provides information about the processes that generate the CERES EBAF-Surface data product and a quality assessment of the product in some details that are not discussed in [the top-of-atmosphere and surface combined data quality summary](#).** For a more thorough description of the methodology used to produce EBAF-Surface, please see Kato et al. (2018). It is strongly suggested that authors, researchers, and reviewers of research papers re-check this document for the latest status before publication of any scientific papers using this data product.

***NOTE: To navigate the document, use Bookmarks in Adobe Reader.  
Select "View > Show/Hide > Navigation Panes > Bookmarks."***

## TABLE OF CONTENTS

<u>Section</u>	<u>Page</u>
1.0 Introduction.....	1
2.0 Description.....	2
2.1 All-sky Surface Flux.....	4
2.1.1 Bias correction .....	4
2.1.1.1 Bias in upper tropospheric temperature (T) and specific humidity (q).....	5
2.1.1.2 Bias in the cloud fraction viewed from space .....	6
2.1.1.3 Bias in the cloud fraction viewed from the surface.....	8
2.1.1.4 Bias in the Terra-derived nighttime cloud fraction for regions 60° poleward .....	9
2.1.2 Lagrange Multiplier .....	10
2.2 Clear-sky Surface Flux .....	11
3.0 Accuracy and Validation.....	13
3.1 Regional mean all-sky surface fluxes.....	13
3.2 Validation by surface observations.....	13
3.3 Comparison at Greenland sites.....	15
3.4 Surface longwave flux during polar nights.....	15
4.0 Known Artifacts.....	17
4.1 Effect of geostationary satellite replacements on surface fluxes.....	17
5.0 References.....	20
6.0 Document Revision Record.....	22

**LIST OF FIGURES**

<u>Figure</u>	<u>Page</u>
Figure 2-1. Top left) Difference of cloud fraction including all cloud types over ocean. The difference is defined as cloud fraction derived from CALIPSO and CloudSat minus MODIS Aqua cloud fraction derived from nadir view only. Top right) Difference of low-level cloud fraction over ocean; Aqua MODIS cloud fraction minus Terra+Aqua MODIS cloud fraction, both derived from all viewing zenith angles. Bottom left) Same as top right but Terra+Aqua MODIS low-level cloud fraction derived from all viewing zenith angles – Terra+Aqua+geostationary satellites (GEOs) low-level cloud fraction. Bottom right) Zonal mean low-level cloud fraction over ocean for Terra+Aqua MODIS + GEOs (TAGI_LOW), Aqua MODIS (AQUA_LOW), Terra+Aqua MODIS (TA_LOW), Aqua MODIS nadir-view only (AQUA_NADIR_LOW), and CALIPSO+CloudSat (CALIP_NADIR_LOW). Zonal cloud fraction difference used for the bias correction is the sum of three black lines shown in top left, top right, and bottom left divided by TAGI_LOW (black line in bottom right). .....	8
Figure 2-2: (top) Downward surface longwave radiative flux correction averaged over polar regions (60° poleward) shown by the solid line. The dashed line indicates the standard deviation derived from corrections applied to 1°×1° regions in polar regions. (bottom) Difference of nighttime cloud fraction derived from MODIS on Aqua and Terra over polar regions. ....	10
Figure 3-1. Difference of EBAF monthly 1°×1° mean surface (top) shortwave and (bottom) longwave downward fluxes from observed fluxes at buoys (computed minus observed). The size of the circle is proportional to the difference. The red and white circles indicate, respectively, a positive and a negative difference. The number of months used for comparisons varies depending on buoys. ....	14
Figure 3-2. Histogram of computed minus observed monthly mean downward shortwave (left) and downward longwave (right) fluxes over the Greenland Summit site. Observed data are provided by Nate Miller. ....	15
Figure 3-3. Time series of downward longwave flux anomalies over the Arctic (60°N - 90°N) and Antarctic (60°S – 90°S). ....	16
Figure 4-1. Anomalies of downward longwave flux in July 2018. Regions with negative anomalies between 90°E to 180°E and 100°W to 40°W over the southern oceans from 30°S to 60°S are affected by the retrieved cloud properties from Himawari-8 and GOES-16, respectively. ....	18
Figure 4-2. Time series of global monthly anomalies of surface (top) downward longwave flux and (bottom) net longwave flux. The net flux is defined as the downward minus upward fluxes. Red arrows indicate months when MTSAT-2 was replaced by Himawari-8 and GOES-13 was replaced by GOES-16 on, respectively, July 6, 2015 and January 1, 2018. ....	19

## LIST OF TABLES

<u>Table</u>	<u>Page</u>
Table 2-1. Data products used for the Edition 4.1 EBAF-Surface product. ....	4
Table 2-2. Fluxes adjusted in the bias correction process. ....	5
Table 2-3. All-sky and clear-sky TOA and surface flux $1\sigma$ uncertainties for $1^\circ \times 1^\circ$ monthly flux adjustment. ....	11
Table 2-4. All-sky and clear-sky $1\sigma$ uncertainties of surface, atmospheric, and cloud properties for $1^\circ \times 1^\circ$ monthly flux adjustment. ....	11
Table 3-1. Uncertainty in regional ( $1^\circ \times 1^\circ$ ) monthly mean irradiances .....	13
Table 3-2. Difference in EBAF surface monthly $1^\circ \times 1^\circ$ mean downward shortwave and longwave fluxes ( $W m^{-2}$ ) from surface observations. Numbers in parentheses are the standard deviations. ....	15

## 1.0 Introduction

To determine the distribution of surface radiation over the globe, the CERES team relies on radiative transfer model calculations initialized using satellite-based cloud and aerosol retrievals and meteorological and aerosol assimilation data from reanalysis to characterize the atmospheric state. The accuracy and stability in computed top-of-atmosphere (TOA) and surface fluxes thus depend upon the quality of the input cloud and atmospheric data (e.g., Rose et al. 2013). The standard CERES data products (e.g., SYN1deg-Month) use cloud and aerosol properties derived from MODIS radiances, meteorological assimilation data from the Goddard Earth Observing System (GEOS) Version 5.4.1 model, and aerosol assimilation from the Model for Atmospheric Transport and Chemistry (MATCH; Collins et al. 2001).

In order to minimize the error in surface fluxes due to uncertainties in the input data sources, the EBAF-Surface data product introduces several additional constraints based upon information from other independent data sources, such as CERES TOA fluxes, AIRS-derived temperature/humidity profiles, and CALIPSO/CloudSat-derived vertical profiles of clouds.

This document describes the procedure used to determine EBAF surface fluxes and provides an assessment of the uncertainty of the EBAF-Surface product.

The overall EBAF data quality summary is found here:

[https://ceres.larc.nasa.gov/documents/DQ\\_summaries/CERES\\_EBAF\\_Ed4.1\\_DQS.pdf](https://ceres.larc.nasa.gov/documents/DQ_summaries/CERES_EBAF_Ed4.1_DQS.pdf)

## 2.0 Description

Surface fluxes in EBAF-Surface are derived from three CERES data products: (i) CERES SYN1deg-Month (Doelling et al. 2013; Rutan et al. 2015) Ed4 provides computed surface fluxes to be adjusted, (ii) CERES EBAF-TOA Ed4.0 (Loeb et al. 2009, Loeb et al. 2012, Loeb et al. 2018) provides the CERES-derived TOA flux constraints by observations, and (iii) SYN1deg-Hour provides weights to compute monthly mean computed clear-sky TOA fluxes.

SYN1deg-Month is a Level 3 product and contains gridded monthly mean computed TOA and surface fluxes along with fluxes at four atmospheric pressure levels (70, 200, 500, and 850 hPa). Surface fluxes in SYN1deg-Month are computed with cloud properties derived from MODIS and geostationary satellites (GEO), where each geostationary satellite instrument is calibrated against MODIS (Doelling et al. 2013). The Ed4 CERES cloud algorithm (Minnis et al. 2018, unpublished manuscript) derives cloud properties (e.g., fraction, optical depth, top height, and particle size) from narrowband radiances measured by MODIS, twice a day from March 2000 through August 2002 (Terra only) and four times a day after September 2002 (Terra plus Aqua). The Edition 4 multi-channel GEO cloud algorithm (Mecikalski et al. 2007; Minnis et al. 2001) provides cloud properties (fraction, top height, optical depth, phase, particle size) at every one hour between Terra and Aqua observations. Cloud properties are gridded onto a  $1^\circ \times 1^\circ$  spatial grid and 1-hourly intervals (hour boxes). Although it occurs less frequently than Ed2.8, cloud properties are missing in some hour boxes. Missing cloud properties are estimated by interpolating between the nearest hour boxes. Up to four cloud-top heights (cloud types: high, mid-high, mid-low, and low) are retained for each hour box within a  $1^\circ \times 1^\circ$  grid box. Cloud properties (cloud top height, optical thickness, particle size, phase, etc.) are kept separately for the four cloud types.

To treat horizontal variability of optical thickness within a cloud type explicitly, both linear and logarithmic means of the cloud optical thicknesses are computed for each cloud type. The distribution of cloud optical thickness expressed as a gamma distribution is estimated from the linear and logarithmic cloud optical thickness means (Barker 1996; Oreopoulos and Barker 1999; Kato et al. 2005). Once the distribution of cloud optical thickness is estimated for each cloud type, a gamma-weighted two-stream radiative transfer model (Kato et al. 2005) is used when the shape factor is less than 10; otherwise, a four-stream model is used to compute the shortwave flux vertical profile for each cloud type. The logarithmic mean optical thickness is used in the longwave flux computation with a modified two-stream approximation (Toon et al. 1989; Fu et al. 1997). The cloud base height, which largely influences the surface downward longwave flux in midlatitude and polar regions, is estimated by an empirical formula described by Minnis et al. (2018, unpublished manuscript).

Temperature and humidity profiles used in the radiative transfer model calculations are from the Goddard Earth Observing System (GEOS-5.4.1) Data Assimilation System reanalysis (Rienecker et al. 2008). Although the GEOS-5.4.1 product has higher temporal and spatial resolutions, the 6-hourly,  $1^\circ \times 1^\circ$  GEOS-5.4.1 temperature and relative humidity profiles are used for surface computations. Skin temperatures used in the computations are at 3-hourly resolution. Column ozone amount is also taken from GEOS-5.4.1. Other inputs used in SYN1deg-Month include ocean spectral surface albedo from Jin et al. (2004). Broadband land surface albedos are inferred from the clear-sky TOA albedo derived from CERES measurements (Rutan et al. 2009). In addition, MODIS spectral radiances over partly cloudy scenes are used to estimate surface albedo over the

clear-sky part of partly cloudy scenes. Emissivity is based on Wilber et al. (1999). Aerosol optical thickness are from an aerosol transport model MATCH (Collins et al. 2001) that assimilates and spatially and temporally interpolates MODIS aerosol optical thickness.

The spectral solar constant used in the shortwave radiative transfer code is Newkur taken from MODTRAN. The solar constant integrated over the entire solar spectral is normalized to match observation provided by the Solar Radiation and Climate Experiment (SORCE) Total Solar Irradiance (TSI) V-15 dataset.

Computed TOA fluxes from SYN1deg-Month do not necessarily agree with the CERES-derived TOA fluxes from EBAF-TOA Ed4.0, partly because of the error in inputs used in the computations and, to a smaller extent, due to assumption in the radiative transfer model. To minimize the error in surface fluxes, we use bias corrections with inputs listed in [Table 2-1](#) and an objective constraint by a Lagrange multiplier algorithm to adjust surface, atmospheric, and cloud properties within their uncertainties in order to ensure that computed TOA fluxes are consistent with the CERES-derived TOA fluxes within their observational errors. The steps involved in the process are follows:

- Determine  $1^\circ \times 1^\circ$  monthly mean differences between the computed TOA fluxes from SYN1deg-Month and the fluxes from CERES EBAF-TOA.
- Correct the TOA longwave bias error caused by the upper tropospheric relative humidity and temperature errors in GEOS-5.4.1 using AIRS (AIRX3STM.006) data. A minor correction also applied to the clear-sky downward longwave flux. We also correct the bias error of the surface downward longwave flux, which is caused by the error in cloud fraction viewed from the surface. In addition, we correct TOA shortwave and longwave, as well as downward and upward surface shortwave fluxes due to the error in the space view cloud fraction. These bias corrections due to surface and space view cloud fractions are based upon the difference between CALIPSO/CloudSat, MODIS and geostationary satellite derived cloud fraction.
- Because of the slow degradation occurring on Terra MODIS bands 27 to 30 that affects the nighttime cloud mask over polar regions, the Terra-derived nighttime cloud fraction over  $60^\circ$  poleward is corrected to match the Aqua-derived nighttime cloud fraction over the same region.
- Use a Lagrange multiplier procedure to determine the perturbation of surface, cloud, and atmospheric properties to match the TOA flux differences, assuming that perturbations applied to the input variables are small relative to their respective monthly mean values. Jacobians that are needed to determine surface, cloud, and atmospheric property perturbations, as well as surface flux adjustments, are computed separately and used in the Lagrange multiplier procedure.
- Compute the surface flux change based on these perturbed surface, cloud, and atmospheric properties. Subsequently, the surface flux changes are added to the  $1^\circ \times 1^\circ$  monthly mean Ed4 SYN1deg-Month fluxes.

Table 2-1. Data products used for the Edition 4.1 EBAF-Surface product.

EBAF Edition	Data product	Use	Time period
Ed 4	AIRX3STM.006 TqJoint grid product	Upper tropospheric temperature and humidity correction	2002-09 to 2016-08
Ed 4	AIRS3STM.006 grid product	Upper tropospheric temperature and humidity correction	2016-09 onward
Ed 4	CCCM B1	Cloud fraction correction	

## 2.1 All-sky Surface Flux

Monthly mean all-sky surface shortwave and longwave fluxes for  $1^\circ \times 1^\circ$  grids are computed by averaging hourly Ed4 SYN1deg all-sky fluxes. We compare monthly  $1^\circ \times 1^\circ$  TOA shortwave and longwave fluxes with those from EBAF-TOA and compute the difference. Based on the differences, we adjust monthly  $1^\circ \times 1^\circ$  upward and downward shortwave and longwave fluxes. As mentioned in the previous section, multiple steps are involved in the process to adjust surface fluxes. Processes are separated into two groups: bias corrections and Lagrange multiplier. We first correct biases to reduce the difference of computed and EBAF TOA shortwave and longwave fluxes before Lagrange multiplier is used. The bias correction also mitigates TOA flux differences to be attributed to atmospheric and cloud properties incorrectly by Lagrange multiplier.

### 2.1.1 Bias correction

Inputs used for computing SYN1deg fluxes are mostly based on observations. When input variables are compared with observations taken by different instruments or derived from other algorithms, some input variables differ significantly. For example, GEOS-5.4.1 upper tropospheric specific humidity is much larger than upper tropospheric specific humidity derived from AIRS. In addition, when thin clouds are screened out, the cloud fraction derived from GEOs is larger than the cloud fraction derived from CALIPSO and CloudSat. A larger upper tropospheric specific humidity reduces computed TOA longwave fluxes, and a larger cloud fraction increases computed TOA shortwave fluxes. The difference between SYN1deg computed and EBAF TOA fluxes are consistent with these biases. Therefore, correcting these biases reduces the difference of computed and EBAF TOA longwave and shortwave fluxes. CALIPSO and CloudSat also provide the occurrence of lower-level clouds present underneath upper-layer clouds that are difficult to observe by MODIS and GEOs. Including lower-level clouds in computing surface fluxes is especially critical for accurate surface downward longwave flux estimates because the downward longwave flux is sensitive to the cloud base height and TOA fluxes do not provide a strong constraint on the surface downward longwave flux.

In addition to these corrections due to biases in temperature, humidity, and cloud fraction, Edition 4.1 corrects the Terra-derived nighttime cloud fraction over the cryosphere ( $60^\circ$  poleward) to match the Aqua-derived nighttime cloud fraction for the same area.

In summary, we consider the bias in temperature (T) and specific humidity (q) between the 200 hPa and 500 hPa levels, cloud fraction viewed from space, and cloud fraction viewed from the surface in the bias correction process. Fluxes adjusted by these bias correction processes are listed in [Table 2-2](#).

All-sky and clear-sky radiative kernels are derived from Ed4 SYN1deg with a temporal resolution of 3-hourly and spatial resolution of  $1^\circ \times 1^\circ$  using 2008 data (Thorsen et al. 2018). The interannual variability of kernels is negligible. We average kernels over a month but maintain the spatial resolution of  $1^\circ \times 1^\circ$ . Cloud kernels are computed for 4 different cloud types (high, mid-high, mid-low, and low) separately.

Table 2-2. Fluxes adjusted in the bias correction process.

Bias correction process	Adjusted fluxes	Resolution and type
Temperature (T) and specific humidity (q) between the 200 hPa and 500 hPa	Clear-sky and all-sky TOA upward longwave fluxes Clear-sky surface downward longwave flux	$1^\circ \times 1^\circ$ , ocean and land using radiative kernels of Thorsen et al. (2018)
Cloud fraction viewed from space	All-sky TOA upward shortwave and longwave fluxes All-sky surface upward and downward shortwave fluxes	$1^\circ \times 1^\circ$ , ocean, using radiative kernels of Thorsen et al. (2018)
Cloud fraction viewed from the surface	All-sky surface downward longwave flux	1-degree zonal with 5-degree smoothing, land and ocean, using radiative kernels of Thorsen et al. (2018)
Nighttime Terra-derived cloud fraction	All-sky surface downward longwave flux	$1^\circ \times 1^\circ$ , $60^\circ$ poleward, using radiative kernels of Thorsen et al. (2018)

### 2.1.1.1 Bias in upper tropospheric temperature (T) and specific humidity (q)

The bias correction of T and q between 200 hPa and 500 hPa is based on the difference of those from GEOS-5.4.1. and derived from AIRS. Although AIRS T and q are not necessarily correct, they are derived from observed TOA spectral radiances. Correcting GEOS-5.4.1 T and q toward those derived from AIRS makes TOA spectral radiance more consistent with observations if spectral radiances were computed. The bias is estimated by comparing monthly mean  $1^\circ \times 1^\circ$  GEOS-5.4.1 T and q in 100 hPa layers between 300 hPa and 500 hPa and 50 hPa layers between 200 hPa and 300 hPa with those from the AIRS level3 version 6 product (AIRX3STM.006, TqJoint grid product). We convert the difference (GEOS-5.4.1 – AIRS) of T and q, layer by layer, to the difference of all-sky and clear-sky TOA longwave fluxes using all-sky and clear-sky radiative kernels. In addition, the surface downward longwave flux is also corrected using clear-sky radiative kernel. Radiative kernels are built by regionally and monthly with no year-to-year variation (i.e. same regional kernel for January of different years). Computed clear-sky TOA

longwave and surface fluxes are subsequently corrected. All-sky surface downward longwave flux is not corrected in this process but it is corrected separately.

AIRS observations are not available before September 2002. We use climatological differences of GEOS-5.4.1 and AIRS monthly  $1^\circ \times 1^\circ$  T and q between 200 hPa and 500 hPa derived from 14 years of data (from September 2002 through August 2015). Similarly, we use climatological clear-sky radiative kernel to convert T and q differences to TOA longwave and surface downward longwave fluxes. Therefore, TOA longwave and surface downward longwave from March 2000 through August 2002 are adjusted using their monthly  $1^\circ \times 1^\circ$  climatological adjustments derived from September 2002 through August 2015.

### 2.1.1.2 Bias in the cloud fraction viewed from space

The bias correction of all-sky TOA shortwave and longwave fluxes and surface downward shortwave fluxes caused by the bias in the cloud fraction viewed from the space involves cloud fraction derived by CALIPSO, CloudSat, MODIS, and GEOs. We correct only low-level cloud fractions over ocean because regions with a larger difference between computed and observed TOA shortwave irradiances are coincide with regions where low-level clouds are often present. In addition, a comparison of cloud fractions derived from MODIS and CALIPSO/CloudSat by cloud type also indicates that the Ed4 MODIS cloud algorithm overestimates the low-level cloud fraction. A further analysis shows that Ed4 GEO cloud algorithms overestimate the low cloud fraction over oceans compared to the low-level cloud fraction derived by the Ed4 MODIS cloud algorithm.

We first estimate the difference of the zonal cloud fraction over ocean derived from MODIS on Aqua and CALIPSO/CloudSat. MODIS cloud fraction is derived over CERES footprints that include the CALIPSO/CloudSat ground track. Therefore, the viewing zenith angle of MODIS is near nadir. Clouds with optical thickness less than 0.3 are excluded from both cloud fractions derived from MODIS (using MODIS-derived optical thickness) and CALIPSO/CloudSat (using CALIPSO-derived extinction profile). We then derive the zonal cloud fraction difference (CC-Aqua) including all cloud types, where CC and Aqua indicate the cloud fraction derived from, respectively, CALIPSO/CloudSat and MODIS on Aqua ([Figure 2-1 top left](#)). When all cloud types are included, the global mean cloud fraction difference averaged over 3 months (January, April, and October 2010) is -0.3. We include all cloud types in comparing MODIS and CALIPSO/CloudSat because, when high- and low-level clouds overlap, MODIS tends to retrieve low-level clouds while the upper-most cloud layer derived from CALIPSO/CloudSat is high-level clouds. A part of the low-level cloud fraction derived from MODIS and CALIPSO/CloudSat is caused by the different instrument footprint sizes. Our further study indicates that the difference in the footprint size leads to the difference in the global mean water cloud fraction difference of about 0.02.

Second, we compute the zonal low-level cloud fractions derived from MODIS on Aqua and on Terra and Aqua ([Figure 2-1 top right](#)) primarily to correct the diurnal cycle of clouds using the full swath, Aqua – (Terra+Aqua). One year of data from 2008 is used to compute the differences. The global mean difference is 0.1.

Third, we compute the zonal low-level cloud fractions derived from Terra MODIS, Aqua MODIS, and GEOs using one year of data in 2008. We then compute the zonal cloud fraction difference of

Terra, Aqua, and GEOs combined to Terra plus Aqua, (Terra+Aqua) – (Terra+Aqua+GEOs) (Figure 2-1 bottom left). The global mean relative low-level cloud fraction difference is -1.8, i.e., GEO-derived cloud fraction is generally larger than MODIS-derived cloud fraction.

Fourth, we simply add these three zonal cloud fraction differences and divide by the zonal mean low-level cloud fraction derived from Terra+Aqua+GEOs (black line shown in bottom right plot in Figure 2-1). We multiply the  $1^\circ \times 1^\circ$  monthly mean low-level cloud fraction over ocean by this relative zonal cloud fraction difference to compute the  $1^\circ \times 1^\circ$  monthly low-level cloud fraction bias. We then use  $1^\circ \times 1^\circ$  monthly cloud fraction kernels computed with Ed4 SYN1deg clouds to convert the cloud fraction bias to TOA shortwave and longwave flux and surface downward shortwave flux biases.

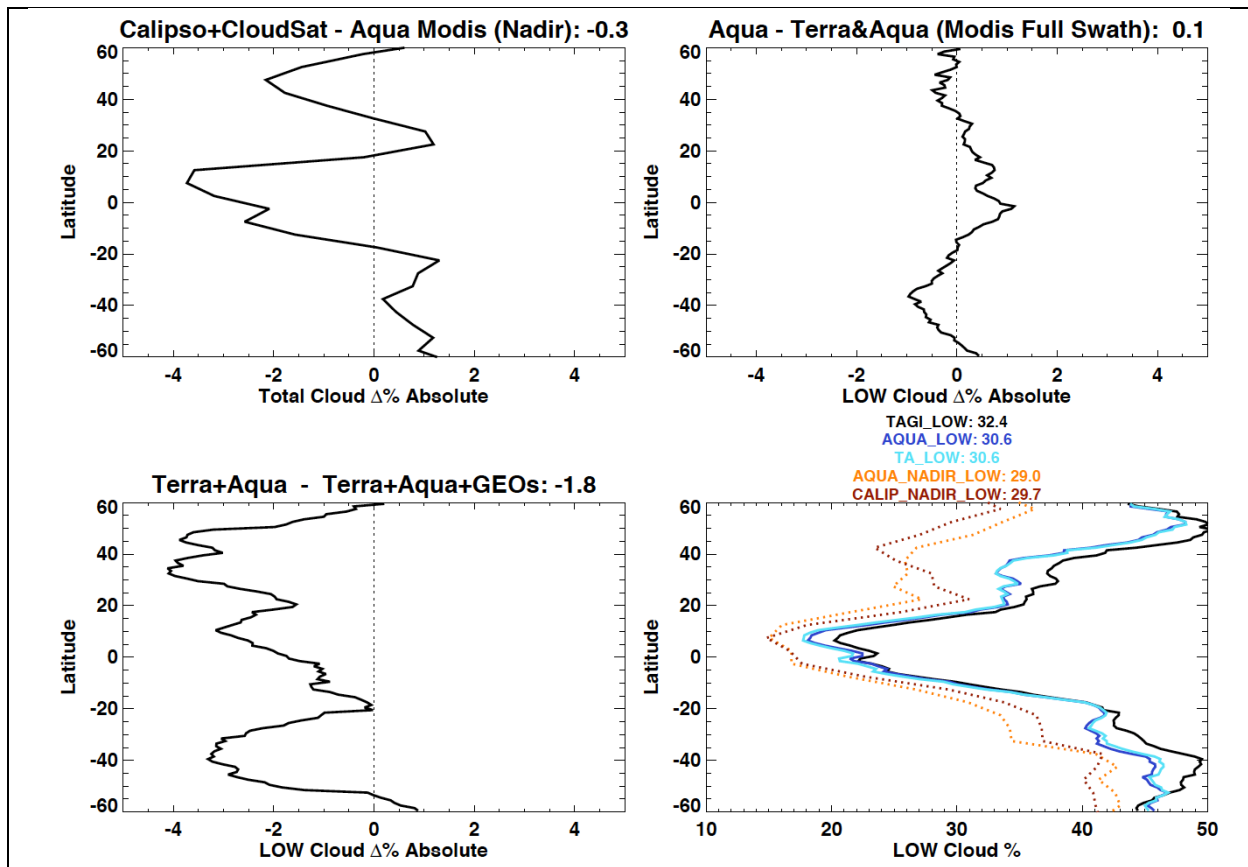


Figure 2-1. Top left) Difference of cloud fraction including all cloud types over ocean. The difference is defined as cloud fraction derived from CALIPSO and CloudSat minus MODIS Aqua cloud fraction derived from nadir view only. Top right) Difference of low-level cloud fraction over ocean; Aqua MODIS cloud fraction minus Terra+Aqua MODIS cloud fraction, both derived from all viewing zenith angles. Bottom left) Same as top right but Terra+Aqua MODIS low-level cloud fraction derived from all viewing zenith angles – Terra+Aqua+geostationary satellites (GEOs) low-level cloud fraction. Bottom right) Zonal mean low-level cloud fraction over ocean for Terra+Aqua MODIS + GEOs (TAGI\_LOW), Aqua MODIS (AQUA\_LOW), Terra+Aqua MODIS (TA\_LOW), Aqua MODIS nadir-view only (AQUA\_NADIR\_LOW), and CALIPSO+CloudSat (CALIP\_NADIR\_LOW). Zonal cloud fraction difference used for the bias correction is the sum of three black lines shown in top left, top right, and bottom left divided by TAGI\_LOW (black line in bottom right).

### 2.1.1.3 Bias in the cloud fraction viewed from the surface

The bias of the surface downward longwave flux is estimated with cloud fraction viewed from the surface. In addition to 4 cloud types (high, high-high, mid-low, and low), Ed4 SYN1deg considers lower-level clouds with a random cloud overlap assumption. This results in the total of 16 different single and two overlapping layer combinations. However, only the four most frequently occurring cloud layer combinations are used in computing surface fluxes in Ed4 SYN1deg for a given  $1^\circ \times 1^\circ$  grid and an hour box. Using the four most frequently occurring cloud layer combinations in Ed4 SYN1deg, we compute zonal cloud fractions viewed from the surface over ocean and land.

Similarly, we compute zonal cloud fractions viewed from the surface from CALIPSO/CloudSat data. We exclude clouds with optical thickness less than 0.3 and a CALIPSO CAD score less than 70. Monthly zonal mean surface view cloud fraction differences over ocean and land separated by cloud type at a 1-degree resolution with 5-degree smoothing are computed using data from January to December 2008. We then convert the bias in zonal monthly mean low-level cloud fraction viewed from the surface (surface view cloud fraction multiplied by relative zonal surface view cloud fraction bias) to the bias in the monthly zonal surface downward longwave flux using zonal cloud fraction kernels derived with Ed4 SYN1deg clouds. Summing up the monthly zonal surface downward longwave flux computed for the four cloud types, we obtain the zonal monthly bias correction for land and ocean separately.

#### **2.1.1.4 Bias in the Terra-derived nighttime cloud fraction for regions 60° poleward**

The bias in the Terra-derived monthly mean nighttime cloud fraction is estimated by comparing with the Aqua-derived monthly mean nighttime cloud fraction over the same area. An assumption is that the Terra- and Aqua-derived nighttime cloud fractions for 60° poleward are the same because of 1) frequent observations by two MODIS instruments at nearly the same time and 2) a small diurnal cycle of nighttime clouds over the region. The correction is derived at a 1°×1° resolution and applied from January 2003. The bottom plot of [Figure 2-2](#) shows that correction of cloud cover averaged over polar regions (60° poleward) by the solid line, i.e., the difference of the nighttime cloud fraction derived from Terra and Aqua MODIS. The cloud fraction difference is converted to the difference of the downward longwave irradiance at the surface using radiative kernel ([Figure 2-2 bottom](#)). We then correct 1°×1° monthly downward longwave irradiance based on the difference.

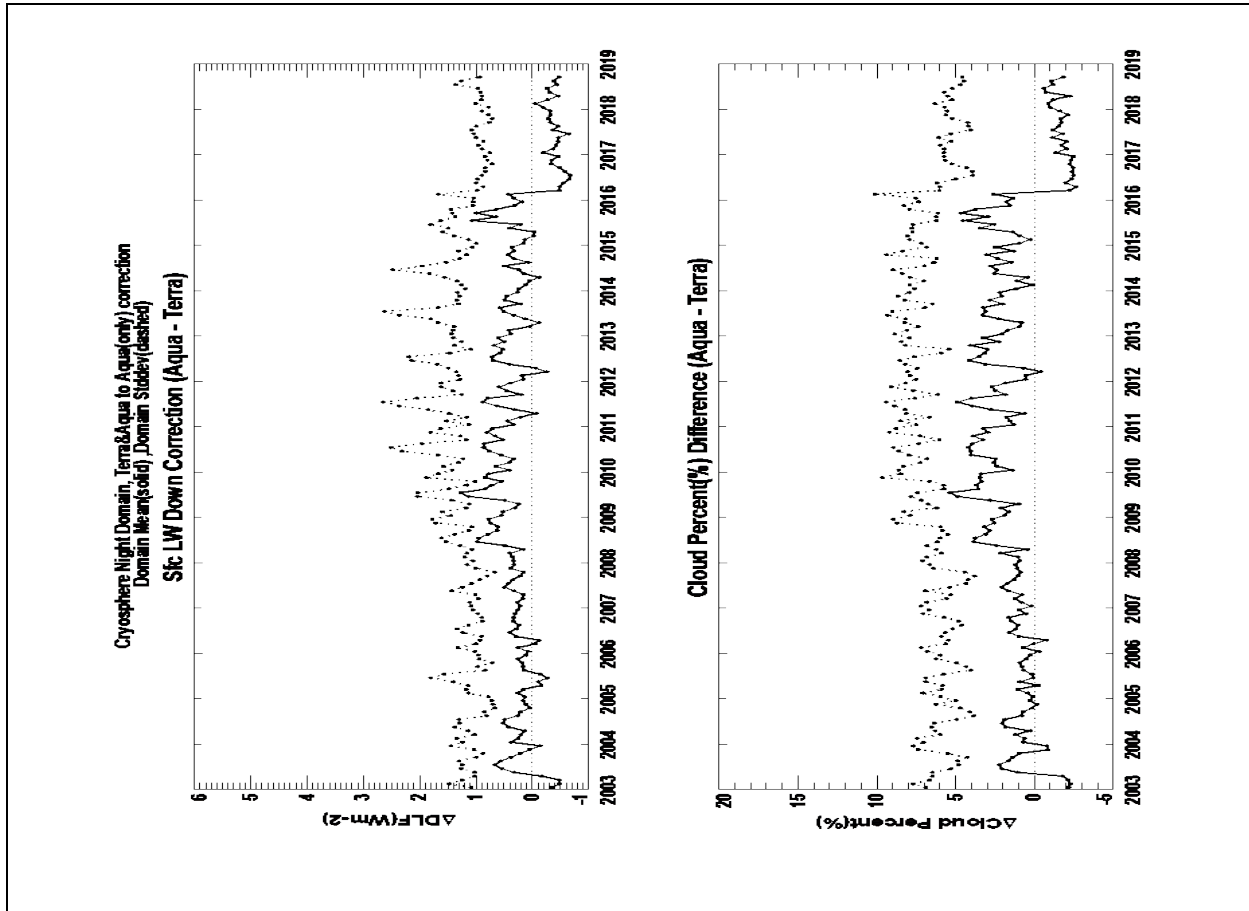


Figure 2-2: (top) Downward surface longwave radiative flux correction averaged over polar regions ( $60^{\circ}$  poleward) shown by the solid line. The dashed line indicates the standard deviation derived from corrections applied to  $1^{\circ} \times 1^{\circ}$  regions in polar regions. (bottom) Difference of nighttime cloud fraction derived from MODIS on Aqua and Terra over polar regions.

### 2.1.2 Lagrange Multiplier

Inputs to the Lagrange multiplier algorithm are modeled and EBAF shortwave and longwave TOA flux differences and their uncertainties. Other inputs are estimated uncertainties of selected input variables used for SYN1deg flux computations.

Here we note that biases exist between EBAF TOA fluxes and those produced in SYN1deg calculations. As discussed in Section 2.1.1, we assume that biases in SYN1deg TOA longwave flux are caused by biases in upper tropospheric T and q, and that biases in TOA shortwave and longwave flux are caused by biases in the space view cloud fraction. We estimate input variable biases based on independent observations (e.g., CALIPSO/CloudSat for cloud fraction and AIRS water vapor for upper tropospheric humidity). Once input variable biases are estimated they are fed into pre-calculated flux kernels (Jacobians) that provide estimates of flux biases. These estimates of the flux bias are subtracted from the difference between Ed4.0 SYN1deg-Month and Ed4.0 EBAF-TOA fluxes, and these differences, along with their uncertainties, are the inputs to the Lagrange multiplier algorithm (Kato et al. 2018). We correct the remaining bias of TOA fluxes

monthly and regionally ( $1^\circ \times 1^\circ$ ). How the components of surface fluxes are adjusted depends on pre-determined uncertainties. Uncertainties used in the Lagrange multiplier process are shown in [Table 2-3](#) and [Table 2-4](#). Partial derivatives of TOA and surface fluxes with respect to atmospheric, cloud, and surface properties (Jacobians) are calculated with monthly mean values with a spatial scale of  $1^\circ \times 1^\circ$ . Jacobians are calculated for clear-sky and all-sky separately.

Table 2-3. All-sky and clear-sky TOA and surface flux  $1\sigma$  uncertainties for  $1^\circ \times 1^\circ$  monthly flux adjustment.

Flux	Uncertainty ( $1\sigma$ )
TOA Shortwave ( $W m^{-2}$ )	0.5
TOA Longwave ( $W m^{-2}$ )	0.5
Surface Downward Shortwave	$1^\circ$ Zonal RMS difference of Ed4 and Ed3 monthly fluxes <sup>1</sup>
Surface Upward Shortwave	$1^\circ$ Zonal RMS difference of Ed4 and Ed3 monthly fluxes <sup>1</sup>
Surface Downward Longwave	$1^\circ$ Zonal RMS difference of Ed4 and Ed3 monthly fluxes <sup>1</sup>
Surface Upward Longwave	$1^\circ$ Zonal RMS difference of Ed4 and Ed3 monthly fluxes <sup>1</sup>

<sup>1</sup>12 seasonal months separated by ocean, land, and cryosphere, all-sky and clear-sky derived based on 2008 to 2011 data.

Table 2-4. All-sky and clear-sky  $1\sigma$  uncertainties of surface, atmospheric, and cloud properties for  $1^\circ \times 1^\circ$  monthly flux adjustment.

Variable	Uncertainty ( $1\sigma$ )
Skin temperature <sup>1</sup>	Monthly $1^\circ \times 1^\circ$ AIRS – GEOS-5.4.1 absolute difference
Surface air temperature <sup>1</sup>	Monthly $1^\circ \times 1^\circ$ AIRS – GEOS-5.4.1 absolute difference
Upper tropospheric relative humidity <sup>1</sup>	Monthly $1^\circ \times 1^\circ$ AIRS – GEOS-5.4.1 absolute difference
Precipitable water <sup>1</sup>	Monthly $1^\circ \times 1^\circ$ AIRS – GEOS-5.4.1 absolute difference
Aerosol optical thickness (relative)	Ocean: 15%, Land: 10%, Cryosphere: 10%
Surface albedo (relative)	Ocean: 1%, Land: 4%, Cryosphere: 8%
Cloud fraction (absolute)	0.05
Cloud optical thickness (relative)	15%
Cloud top pressure (hPa)	10
Cloud base pressure (hPa)	10

<sup>1</sup>Uncertainty value varies depending on month and  $1^\circ \times 1^\circ$  region.

## 2.2 Clear-sky Surface Flux

The bias correction and Lagrange multiplier process for clear sky are the same as those for all-sky processes. The clear-sky flux adjustment involves an additional process to make the sampling of computed fluxes consistent with observed clear-sky fluxes. Monthly mean clear-sky surface shortwave and longwave fluxes  $\langle F \rangle$  are computed by averaging daily hourly Ed4 SYN1deg clear-sky fluxes (i.e., averaging hourly fluxes of the same hour in a day over a month) that are computed

by removing clouds weighted by the clear fraction over a  $1^\circ \times 1^\circ$  grid box to form monthly mean hourly fluxes and averaging monthly hourly fluxes,

$$\langle F \rangle = \frac{1}{n_{hour}} \sum_{i=1}^{n_{hour}} \frac{\sum_{j=1}^{n_{day}} w_{ij} F_{ij}}{\sum_{i=1}^{n_{hour}} \sum_{j=1}^{n_{day}} w_{ij}},$$

where  $w_{ij}$  is the clear fraction at  $i$ -th hour on  $j$ -th day in the month, and  $F_{ij}$  is either hourly mean shortwave or longwave fluxes. For longwave fluxes,  $\langle F_{LW} \rangle = \langle F \rangle$ . For shortwave irradiances, the insolation correction ratio  $\langle R \rangle$  is computed by

$$\langle R \rangle = \frac{\sum_{i=1}^{n_{hour}} \sum_{j=1}^{n_{day}} F_{0,ij} / (n_{day} n_{hour})}{\sum_{i=1}^{n_{hour}} \sum_{j=1}^{n_{day}} w_{ij} F_{0,ij} / \left( n_{hour} \sum_{j=1}^{n_{day}} w_{ij} \right)},$$

where  $F_0$  is the solar constant and  $\langle F_{sw} \rangle = \langle R \rangle \langle F \rangle$ . The clear-sky fraction is derived from MODIS. The cloud fraction for hour boxes with no MODIS observations is derived by interpolating MODIS-derived clear fraction.

Clear-sky TOA longwave and surface downward longwave flux biases due to upper tropospheric temperature and specific humidity are corrected by the process explained in Section 2.1 (All-sky surface flux).

### 3.0 Accuracy and Validation

Uncertainties in surface fluxes at various temporal and spatial scales are estimated by Kato et al. (2018). In this section, we update the uncertainties given in Kato et al. (2013) with surface fluxes from Ed4 EBAF-Surface.

#### 3.1 Regional mean all-sky surface fluxes

We assume that the random error is caused by uncertainties in the variables shown in Table 2-4. The bias correction made due to the estimated bias in upper tropospheric relative humidity and cloud fraction viewed from space and surface is treated as a  $1\sigma$  uncertainty. In addition, the uncertainties shown in Table 2-4 that are used in the Lagrange multiplier are treated as random  $1\sigma$  errors. We convert these uncertainties to surface irradiance uncertainties using radiative kernels. All components are assumed to be independent.

We compare the uncertainty calculated from uncertainty in input variables with the RMS error of computed and observed surface fluxes (Table 3-1). We will use the larger value for a given surface type (e.g., land, ocean, Arctic, and Antarctic) as the uncertainty.

Table 3-1. Uncertainty in regional ( $1^\circ \times 1^\circ$ ) monthly mean irradiances

	Shortwave ( $\text{W m}^{-2}$ )		Longwave ( $\text{W m}^{-2}$ )	
	Downward	Upward	Downward	Upward
Ocean	11	11	5	13
Land	13	12	10	19
Arctic ( $60^\circ\text{N}$ - $90^\circ\text{N}$ )	14	16	12	12
Antarctic ( $60^\circ\text{S}$ - $90^\circ\text{S}$ )	21	24	12	13

#### 3.2 Validation by surface observations

Figure 3-1 shows the difference of EBAF monthly  $1^\circ \times 1^\circ$  mean surface (top) shortwave and (bottom) longwave downward fluxes from observed fluxes at buoys (computed minus observed). The mean difference on monthly mean fluxes averaged for 49 buoy sites is  $4.9 \text{ W m}^{-2}$  for downward shortwave and  $1.1 \text{ W m}^{-2}$  for downward longwave with the standard deviation of, respectively,  $10.5 \text{ W m}^{-2}$  and  $4.7 \text{ W m}^{-2}$ . Larger differences over tropical Atlantic Ocean is caused by accumulation of dusts transported from Africa on buoys (Foltz et al. 2013). The bias of downward shortwave flux can exceed  $-40 \text{ W m}^{-2}$  in a monthly mean for buoys located in the high-dust region ( $8^\circ$ ,  $12^\circ$ , and  $15^\circ\text{N}$  along  $38^\circ\text{W}$ ;  $12^\circ$  and  $21^\circ\text{N}$  along  $23^\circ\text{W}$ ), while mean bias is of the order of  $-10 \text{ W m}^{-2}$ .

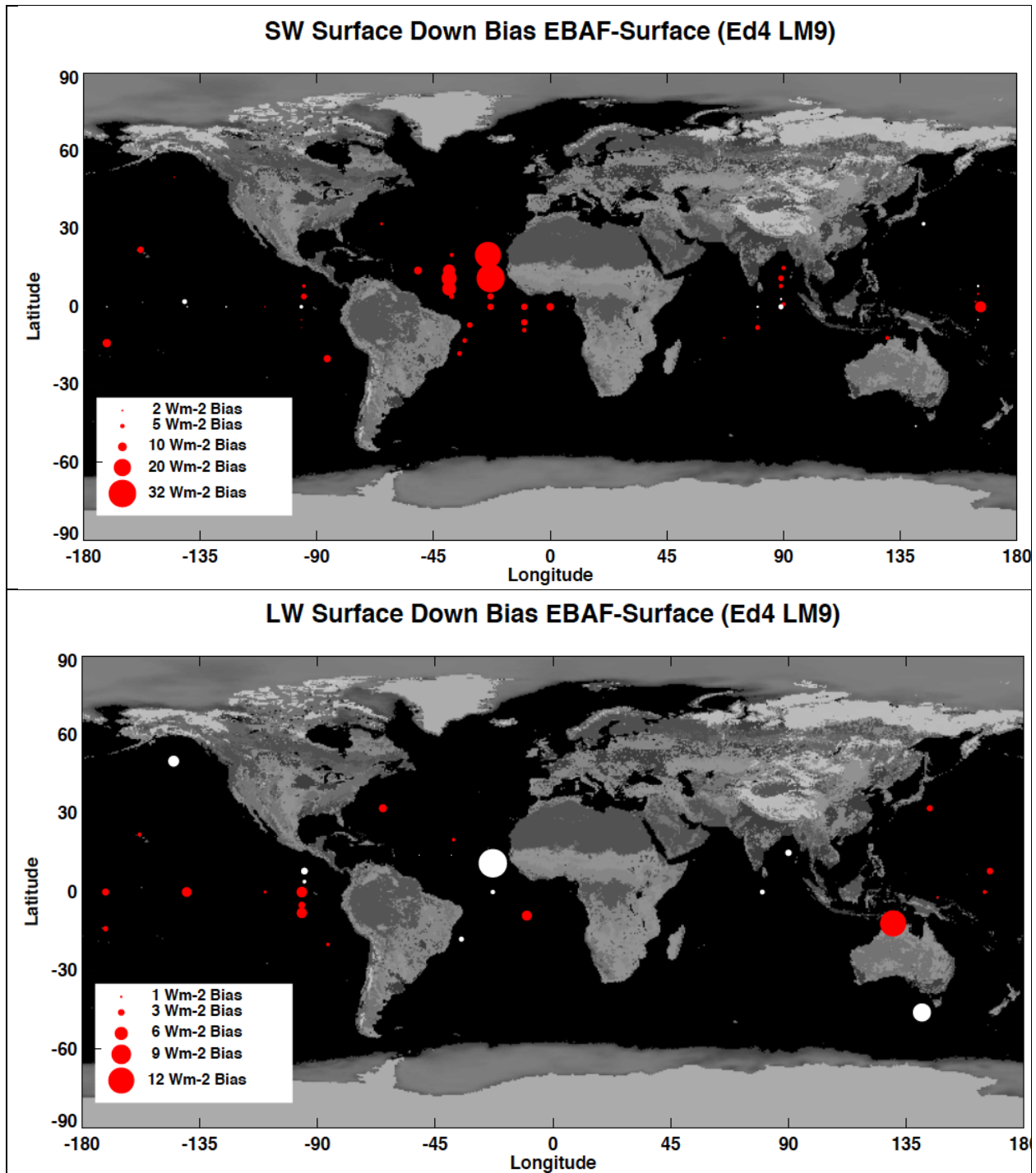


Figure 3-1. Difference of EBAF monthly  $1^{\circ} \times 1^{\circ}$  mean surface (top) shortwave and (bottom) longwave downward fluxes from observed fluxes at buoys (computed minus observed). The size of the circle is proportional to the difference. The red and white circles indicate, respectively, a positive and a negative difference. The number of months used for comparisons varies depending on buoys.

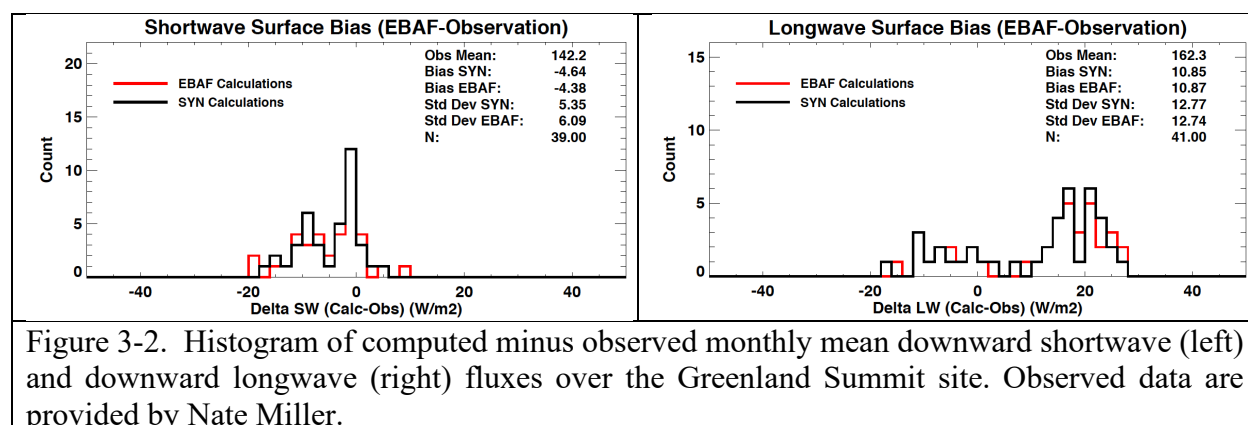
Comparisons with surface observations by surface type are shown in [Table 3-2](#). Buoys in the tropical Atlantic Ocean that have large biases due to African dust are excluded in computing the statistics shown in here.

Table 3-2. Difference in EBAF surface monthly  $1^{\circ} \times 1^{\circ}$  mean downward shortwave and longwave fluxes ( $W m^{-2}$ ) from surface observations. Numbers in parentheses are the standard deviations.

	<b>Downward Shortwave</b>	<b>Downward Longwave</b>
All sites (85 sites)	1.98 (12.64)	0.08 (9.21)
Ocean buoys	4.67 (10.65)	1.19 (4.84)
Land	-0.74 (11.59)	0.04 (9.76)
Arctic	3.74 (13.15)	0.43 (12.34)
Antarctic	-4.07 (20.13)	3.14 (11.73)

### 3.3 Comparison at Greenland sites

Downward surface shortwave fluxes are biased negatively by  $4 W m^{-2}$  and downward surface longwave fluxes are biased positively by  $11 W m^{-2}$  compared with observation taken at the Summit (SMT) ([Figure 3-2](#)). This is primarily due to a positive bias of cloud fraction over high elevation regions. In particular, low-mid and high-mid cloud fractions are biased high over the Summit site except for summertime. The effect of the positive bias of cloud fraction on surface radiative fluxes for other polar regions is less pronounced ([Table 3-1](#)).



### 3.4 Surface longwave flux during polar nights

Because of the degradation of Terra MODIS water vapor channel that is used to detect clouds mostly at high altitude in polar regions during polar nights, the nighttime cloud fraction over Antarctica derived from Terra MODIS is about 2% less than the nighttime cloud fraction derived from Aqua MODIS over the same region. The effect of the degradation on the surface downward longwave flux becomes apparent around 2008. A large drop of cloud fraction derived from Terra MODIS over the Antarctica occurs in March 2016. The mitigation of the impact of downward longwave flux over cryosphere has been implemented in Ed 4.1.

Because of the degradation of the Terra water vapor channel, the time series of downward longwave flux anomalies and net longwave flux anomalies over polar regions (60N to 90N and 60S to 90S) shows a downward trend (Figure 3-3). For this reason, trend analyses with surface fluxes over polar regions from Ed4.0 EBAF-Surface should be avoided.

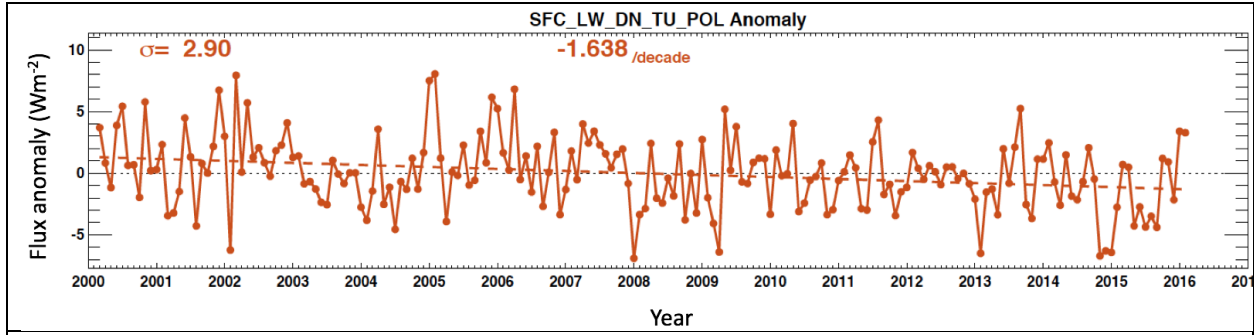


Figure 3-3. Time series of downward longwave flux anomalies over the Arctic (60°N - 90°N) and Antarctic (60°S - 90°S).

## 4.0 Known Artifacts

In this section, we describe known artifacts occurring in Edition 4.1 EBAF-Surface fluxes. This section will be updated as new artifacts are determined. When one analyzes surface flux changes, one should be aware of the artifacts described in this section.

### 4.1 Effect of geostationary satellite replacements on surface fluxes

Replacements of geostationary satellites affect retrieved cloud properties. The exact magnitude and which cloud properties are affected by a replacement depend on the cloud type. Therefore, depending on the occurrence of certain cloud types, an apparent discontinuity may not coincide with the month when a geostationary satellite was replaced. However, because a replacement generally affects cloud properties systematically, it can affect the time series of global monthly anomalies of surface irradiances. Although the exact magnitude is difficult to quantify, we document in this section the potential impacts of replacements of MTSAT-2 by Himawari-8 and GOES-13 by GOES-16 on the downward longwave and net longwave fluxes.

[Figure 4-1](#) shows the spatial distribution of downward longwave flux anomalies in July 2018. Cloud properties for regions between 90°E and 180°E were derived from Himawari-8 and between 100°W to 40°W were derived from GOES-16. The use of all geostationary satellites is limited to 60°N to 60°S. Because more channels are used for the retrievals from these satellites compared to the retrieval from previous geostationary satellites over the same regions, retrieved cloud emissivity decreased and cloud top height increased when the geostationary satellites were switched to Himawari-8 and GOES-16. As a result, negative anomalies in the downward longwave flux appear over a large area. Some anomalies shown in the region of 90°E to 180°E and 100°W to 40°W between 30°S to 60°S are real, but geostationary artifacts with sharp longitudinal discontinuities are apparent. The exact magnitude of changes caused by the switches is, however, difficult to quantify. Although the effect on the time series of global monthly anomalies of downward longwave fluxes and net longwave fluxes is not clearly apparent ([Figure 4-2](#)), as more existing geostationary satellites are replaced by new generation geostationary satellites, the effect might become more apparent.

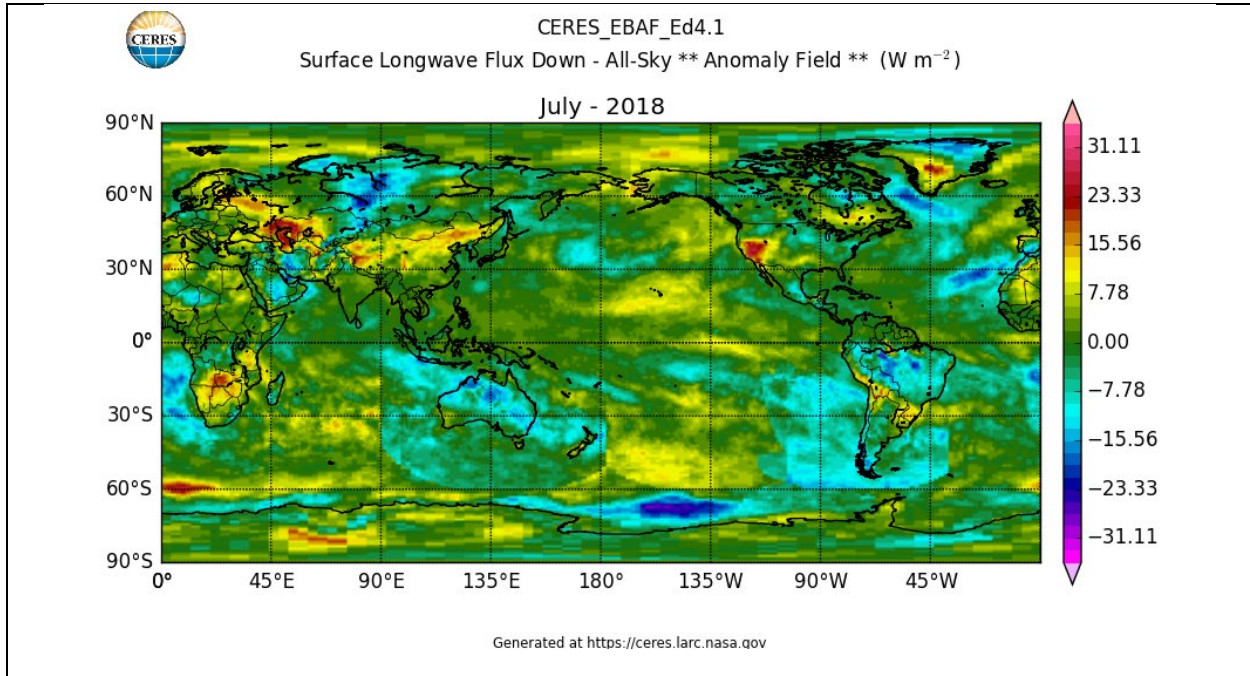


Figure 4-1. Anomalies of downward longwave flux in July 2018. Regions with negative anomalies between 90°E to 180°E and 100°W to 40°W over the southern oceans from 30°S to 60°S are affected by the retrieved cloud properties from Himawari-8 and GOES-16, respectively.

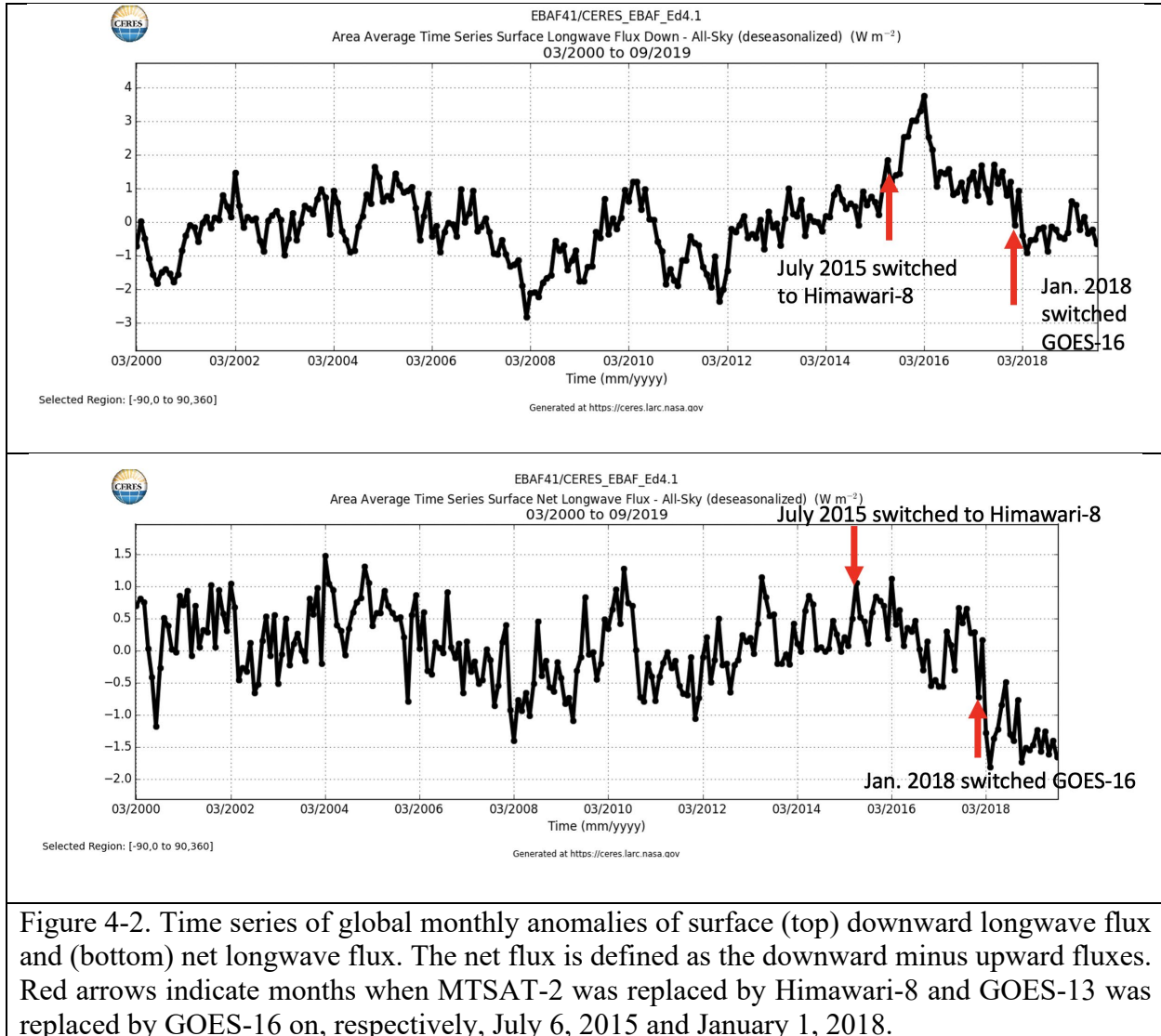


Figure 4-2. Time series of global monthly anomalies of surface (top) downward longwave flux and (bottom) net longwave flux. The net flux is defined as the downward minus upward fluxes. Red arrows indicate months when MTSAT-2 was replaced by Himawari-8 and GOES-13 was replaced by GOES-16 on, respectively, July 6, 2015 and January 1, 2018.

## 5.0 References

- Barker, H. W., 1996: A parameterization for computing grid-averaged solar fluxes for inhomogeneous marine boundary layer clouds. Part I: Methodology and homogeneous biases. *J. Atmos. Sci.*, **53**, 2289-2303.
- Collins, W. D., P. J. Rasch, B. E. Eaton, B. V. Khatatov, J.-F. Lamarque, and C. S. Zender, 2001: Simulating aerosols using a chemical transport model with assimilation of satellite aerosol retrievals: Methodology for INDOEX. *J. Geophys. Res.*, **106**, 7313–7336.
- Doelling, D. R., N. G. Loeb, D. F. Keyes, M. L. Nordeen, D. Morstad, C. Nguyen, B. A. Wielicki, D. F. Young, and M. Sun, 2013: Geostationary enhanced temporal interpolation for CERES flux products, *J. Atmos. Oceanic Technol.*, **30**, 1072-1090, doi:10.1175/JTECH-D-12-00136.1.
- Foltz, G. R., A. T. Evan, H. P. Freitag, S. Brown, M. McPhaden, 2013: Dust accumulation biases in PIRATA shortwave radiation records, *J. Atmos. Ocean. Tech.*, **30**, doi: 10.1175/JTECH-D-12-00169.1.
- Fu, Q., K. Liou, M. Cribb, T. Charlock, and A. Grossman, 1997: On multiple scattering in thermal infrared radiative transfer. *J. Atmos. Sci.*, **54**, 2799-2812.
- Jin, Z., T. P. Charlock, W. L. Smith, Jr., and K. Rutledge, 2004: A look-up table for ocean surface albedo. *Geophys. Res. Lett.*, **31**, L22301.
- Kato, S., F. G. Rose, and T. P. Charlock, 2005: Computation of domain-averaged irradiance using satellite derived cloud properties. *J. Atmos. Oceanic Technol.*, **22**, 146-164.
- Kato, S., N. G. Loeb, F. G. Rose, D. R. Doelling, D. A. Rutan, T. E. Caldwell, L. Yu, and R. A. Weller, 2013: Surface irradiances consistent with CERES-derived top-of-atmosphere shortwave and longwave irradiances, *J. Climate*, **26**, 2719-2740, doi:10.1175/JCLI-D-12-00436.1.
- Kato, S., F. G. Rose, D. A. Rutan, T. E. Thorsen, N. G. Loeb, D. R. Doelling, X. Huang, W. L. Smith, W. Su, and S.-H. Ham, 2018: Surface irradiances of Edition 4.0 Clouds and the Earth's Radiant Energy System (CERES) Energy Balanced and Filled (EBAF) data product, *J. Climate*, **31**, 4501-4527, doi:10.1175/JCLI-D-17-0523.1.
- Loeb, N. G., B. A. Wielicki, D. R. Doelling, G. L. Smith, D. F. Keyes, S. Kato, N. Manalo-Smith, and T. Wong, 2009: Toward optimal closure of the Earth's top-of-atmosphere radiation budget. *J. Climate*, **22**, 748-766.
- Loeb, N. G., J. M. Lyman, G. C. Johnson, R. P. Allan, D. R. Doelling, T. Wong, B. J. Soden, and G. L. Stephens, 2012: Observed changes in top-of-the-atmosphere radiation and upper-ocean heating consistent within uncertainty. *Nat. Geosci.*, **5**, 110-113. doi:10.1038/NGEO1375.
- Loeb, N. G., D. R. Doelling, H. Wang, W. Su, C. Nguyen, J. G. Corbett, L. Liang, C. Mitrescu, F. G. Rose, and S. Kato, 2018: Clouds and the Earth's Radiant Energy System (CERES) Energy Balanced and Filled (EBAF) Top-of-Atmosphere (TOA) Edition-4.0 data product. *J. Climate*, **31**, 895-918, doi: 10.1175/JCLI-D-17-0208.1.

- Mecikalski, J. R., and Coauthors, 2007: Aviation applications for satellite-based observations of cloud properties, convective initiation, in-flight icing, turbulence, and volcanic ash. *Bull. Amer. Meteor. Soc.*, **88**, 1589–1607.
- Minnis, P., and Coauthors, 2001: A near real time method for deriving cloud and radiation properties from satellites for weather and climate studies. *Proc. 11th Conf. Satellite Meteorology and Oceanography*, Madison, WI, Amer. Meteor. Soc., 477–480.
- Oreopoulos, L. and H. W. Barker, 1999: Accounting for subgrid-scale cloud variability in a multi-layer 1D solar radiative transfer algorithm. *Quart. J. Roy. Meteor. Soc.*, **125**, 301-330.
- Rienecker, M. M. and Coauthors, 2008: The GOES-5 Data Assimilation System-Documentation of Versions 5.0.1, 5.1.0, and 5.2.0. NASA Tech. Rep. NASA/TM-2009-104606, Vol. 27, 118 pp.
- Rose, F., D. A. Rutan, T. P. Charlock, G. L. Smith, and S. Kato, 2013: An algorithm for the constraining of radiative transfer calculations to CERES-observed broadband top-of-atmosphere irradiance, *J. Atmos. Oceanic Technol.*, **30**, 1091-1106, doi:10.1175/JTECH-D-12-00058.1.
- Rutan, D., F. Rose, M. Roman, N. Manalo-Smith, C. Schaaf, and T. Charlock, 2009: Development and assessment of broadband surface albedo from Clouds and the Earth's Radiant Energy System clouds and radiation swath data product. *J. Geophys. Res.*, **114**, D08125, doi:10.1029/2008JD010669.
- Rutan, D. A., S. Kato, D. R. Doelling, F. G. Rose, L. T. Nguyen, T. E. Caldwell, and N. G. Loeb, 2015: CERES synoptic product: Methodology and validation of surface radiant flux. *J. Atmos. Oceanic Technol.*, **32**, 1121–1143, doi:10.1175/JTECH-D-14-00165.1.
- Thorsen, T. J., S. Kato, N. G. Loeb, and F. G. Rose, 2018: Observation-based decomposition of radiative perturbations and radiative kernels. *J. Climate*, **31**, 10039–10058, doi:10.1175/JCLI-D-18-0045.1.
- Toon, O. B., C. P. McKay, T. P. Ackerman and K. Santhanam, 1989: Rapid calculation of radiative heating rates and photodissociation rates in inhomogeneous multiple scattering atmospheres. *J. Geophys. Res.*, **94**, 16 287–16 301.
- Wilber, A. C., D. P. Kratz, and S. K. Gupta, 1999: Surface emissivity maps for use in satellite retrievals of longwave radiation. NASA Tech. Memo. TP-1999-209362, 30 pp.

## 6.0 Document Revision Record

The Document Revision Record contains information pertaining to approved document changes. The table lists the Version Number, the date of the last revision, a short description of the revision, and the revised sections.

Document Revision Record

<b>Version Number</b>	<b>Date</b>	<b>Description of Revision</b>	<b>Section(s) Affected</b>
V1	06/08/2021	<ul style="list-style-type: none"><li>Existing document put in version control.</li></ul>	All